

The effects of He plasma interactions with SiH₄ in remote plasma enhanced chemical vapor deposition

Jeremy A. Theil^{a)} and Gary Powell

Departments of Physics, and Materials Science and Engineering, North Carolina State University, Raleigh, North Carolina 27695-8202

(Received 13 August 1993; accepted for publication 12 November 1993)

Plasma generation and the effects of the plasma on SiH₄ are examined for the remote plasma enhanced chemical vapor deposition (remote PECVD) process. The electrical characteristics of two plasma generation techniques using He were compared, one at 13.56 MHz and the other at 2.45 GHz. It has been shown that the plasma generation technique has an effect upon the power coupling to the discharge in that the 13.56 MHz technique yields a capacitively coupled discharge, while the 2.45 GHz technique yields an inductively coupled discharge. There are two distinguishable methods for generating charged species in the main portion of the reactor for 13.56 MHz discharges, electron impact ionization, and Penning ionization. What has been demonstrated is that SiH₄ forms polysilanes as a direct consequence of interactions with charge created with the capacitively coupled discharge (13.56 MHz) by forming polysilanes, however Penning ionizations cannot sustain appreciable gas-phase SiH₄ excitation. These polysilanes account for a significant fraction of the SiH₄ in the reactor. In fact, due to the chemical similarity of these polysilanes and their concentration relative to SiH₄, they should be considered in models of silicon thin-film growth in remote PECVD. Hydrogen has been shown to reduce the presence of polysilane species in the plasma for conditions that are conducive to microcrystalline Si growth, and cause silane species to exhibit a higher degree of hydrogenation.

I. INTRODUCTION

Remote plasma enhanced chemical vapor deposition has been used to grow many types of silicon-based thin films using SiH₄ as the silicon source gas.¹⁻⁶ The two main classifications of film growth deposition schemes are (1) silicon-based semiconductor film growth in which a SiH₄ compound and other gases containing nondeposition elements are injected, and (2) dielectric film growth in which a second-atom-source gas is also injected into the reactor.^{2,5,6} In the first case, the gaseous products of plasma interactions are only other silane-based compounds. However, from SiH₄ there are many forms of semiconducting silicon that can be grown. By altering the SiH₄ concentration, plasma generation method, and Si:H ratio in the gas phase, the microstructure, electrical properties, and hydrogen content can be varied. Therefore developing an understanding of how the plasma is generated and how SiH₄ interacts with the plasma will be a crucial step in developing film growth processes. This article characterizes the plasma generated by the remote plasma enhanced chemical vapor deposition PECVD system, and how the results of plasma SiH₄ interactions affect film growth.

The topics considered in this article concern issues of generation of discharges in the remote PECVD reactor, SiH₄ interactions with the discharge afterglow, and the products of the SiH₄ interactions. For plasma-driven techniques, charged species produced by the plasma are known to be directly involved in certain deposition reactions, and

indirectly responsible for others.⁷⁻⁹ It was found that the 2.45 GHz He discharge was not able to support measurable excitation with SiH₄, so only its electrical characterization is compared to the 13.56 MHz discharge. Excitation frequency and power application geometry can affect the mode of power coupling with the plasma and to a large extent determine the spatial and energy distribution for the majority of electrons. It is also recognized that the method of charge generation greatly influences the discharge characteristics, and hence the possible reaction pathways. Data will be presented that demonstrates more than one charge generation mechanism is present in the reactor. Additions of H₂ to the reactor alter the relative concentrations of SiH₄ fragments and ensure hydrogen termination of silicon surfaces. The degree of hydrogen termination determines the surface reactions that lead to network propagation. For example, Tanaka and Matsuda showed that as the silicon surface loses surface bound hydrogen, the films change from a microcrystalline structure to an amorphous morphology.¹⁰ It is known that H₂ promotes crystalline phase formation from PECVD processes and that it plays a key role in surface processes on the substrate and on the growing film. The addition of H₂ suppresses production of certain species.

Since SiH₄ is the source of silicon in most of the reaction systems studied for remote PECVD deposition of Si-based thin films, a clear picture of the SiH₄ consumption paths is necessary. While unreacted SiH₄ and silicon film growth have been considered the only reaction channels for SiH₄ in remote PECVD, evidence will be presented that shows gas-phase polymerization of SiH₄ must also be considered.¹¹

Three *in situ* analytical techniques were employed in

^{a)} Author to whom correspondence should be addressed: Central Research Laboratories (G3), Johnson Controls, Inc., 5757 N. Green Bay Ave., Milwaukee, WI 53209.

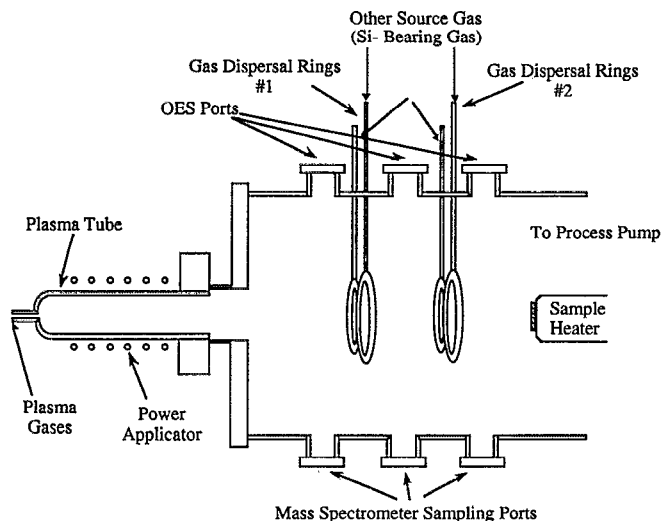


FIG. 1. Schematic diagram of 15 cm diam reactor.

order to characterize the discharge and SiH_4 interactions with the plasma: (1) double Langmuir probe, to detect the charged species within the reaction chamber, (2) mass spectrometry, to measure changes in the concentration gaseous products of plasma and electron impact excitation of SiH_4 , and (3) optical emission spectroscopy to detect radiating metastable species. The double Langmuir probe technique characterized the electrical properties of the discharge and demonstrated differences in the coupling of the two generation techniques. The mass spectrometry was used to show the consumption of SiH_4 , and the presence of polysilane species in the discharge. Optical emission spectroscopy showed how the optical states of He and SiH_4 changed under varying processing conditions, as well as comparing n_e with relative changes in metastable concentrations.

II. EXPERIMENT

The chamber used in these experiments has a 14.9 cm inner diameter and 56 cm length, see Fig. 1. At one end is a plasma tube flange in which a 3.2 cm inner diameter fused silica tube is located on the central chamber axis. Inside the chamber, at 10.2 and 35.6 cm from the end of the plasma tube, are two sets of double stainless steel gas rings welded to a conflat flange for downstream injection of gases. The mass spectrometer sampling stations are located 3.5 cm downstream from the plasma tube flange, position No. 1, and 3.8 cm downstream from each of the gas injection rings, positions No. 2 (14.0 cm) and No. 3 (39.4 cm), respectively. Each station has three ports, two horizontal ones with pyrex windows, and a vertical one to accommodate the sniffer tube for the mass spectrometer. A Leybold TMP360H turbomolecular pump services the chamber from a vertically mounted 6 in. flange located 25 cm downstream from the plasma tube, capable of achieving a base pressure of $\sim 3 \times 10^{-8}$ Torr.

Two excitation frequencies were used for this research, 13.56 MHz, and 2.45 GHz. The 13.56 MHz antenna is a

ten-turn 4.45 cm inner diameter copper coil wrapped around the plasma tube. The coil is soldered to a coaxial connector and mounted within a grounded metal box with two 4.45 cm diam openings for the plasma tube. The 13.56 MHz power is delivered from an rf generator through a coaxial cable via a matching network (Plasma Products model HFS-251 power supply, and MN-500 matching network). The antenna is housed in an aluminum box mounted on the chamber by stainless steel rods. The antenna terminates in the air, without any connection to ground.

The 2.45 GHz system is a commercially available unit consisting of an ASTEX S-250 power supply capable of generating a 0–250 W signal and standard dimension waveguide components for the 2.45 GHz band (TE_{01} waveguide transmission mode).¹² The transmission components are arranged with a circulator and a dummy load bolted to the output flange of the power supply, and a waveguide-to-coaxial converter attached to the output side of the circulator. The coaxial cable is connected to another converter that is attached to two 50 db directional couplers. A network matching three-stub tuner connects the directional couplers with the applicator. The applicator is a section of waveguide with a 3.8 cm diam opening, two resonant A1 wings for the plasma tube, and a tuned shunt termination. The applicator waveguide is supported by a rigid channel-bar A1 stock mounting frame to prevent movement of the applicator and damage to the plasma tube. The gas stem nipple of the plasma tube is supported by a frame mounted holder that permits three axis alignment.

Electrical characterization of the plasma was made with the double Langmuir probe. The technique utilizes two conductors in contact with the plasma so that a complete current path irrespective of ground may be completed. This minimizes the disturbance of the plasma by minimizing displacement charge and allows the electrodes to follow the varying electric field of rf plasmas.¹³ The probe head consists of a 0.953 cm diam pyrex tube, approximately 10 cm long with two platinum electrodes encased in 1 mm pyrex sheaths. The probes protrude from the end of the tube with a probe-to-probe spacing of 7 mm. The electrode dimensions are 0.56 mm (24 gauge) diam \times 1.91 cm long. The exposed probe leads adjacent to the glass seal are covered with a $3 \times 1 \text{ mm}^2$ alumina insulator. The probes are mounted on the baseplate that is a retractable rod that can be positioned anywhere along the axis of the chamber, from just inside the mouth of the plasma tube to the load lock. The electrical connections are made from stainless steel conductors of the vacuum feedthrough and probes with copper connectors in the space behind the baseplate. The connections are covered with a specially fitted copper cylinder ground shield. The leads are joined to two external single strand coaxial copper wires that run the length of the 91 cm stainless steel feedthrough. The coaxial ground shielding is tied to the driven-guard connectors of the triaxial pickup cables that connect to the Keithley 237 source measurement unit. It should be noted that there was no decoupling of the Langmuir probe from the source measurement unit. T_e is found from an analysis

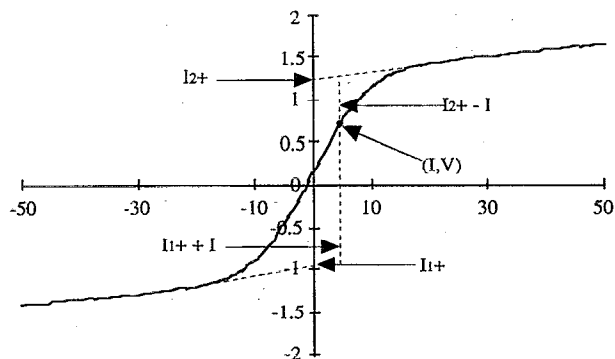


FIG. 2. Diagram of double Langmuir probe I - V characteristic.

of the double probe curve by examining the dependence of current collection as a function of the applied potential

$$T_e = \frac{e}{k} \frac{I_1 + I_2}{I_1 + I_2} \left(\frac{dI}{dV} \bigg|_0 \right)^{-1}, \quad (1)$$

where the derivative is the slope of the I - V curve at $V=0$ V, and I_{1+} and I_{2+} are the magnitudes of the saturation current in both directions of the trace (see Fig. 2). For order of magnitude n_e estimates, the Bohm, Burhop, and Massey equation was used.¹⁴

The default conditions used for the Langmuir probe experiments were He discharges, 200 sccm total gas flow through the plasma tube, and a pressure of 300 mTorr. No SiH_4 was injected into the chamber during measurements to prevent probe contamination. The power was maintained at 25 W for 13.56 MHz, and 170 W for 2.45 GHz. The high microwave power level was required to maintain the 2.45 GHz discharge within the waveguide applicator due to difficulties in impedance matching caused by the inserted coaxial cable and the high ionization potential of the He feedstock gas.

The chemical characterization of the reactor gas was made by mass spectrometry and optical emission spectroscopy. The quadrupole mass spectrometer is an EXTREL model C50 housed in a custom-built 10.2 cm diam stainless steel chamber with dedicated backing pumps, a Leybold TMP360V turbomolecular pump, and a Leybold D4B rotary vane pump (see Fig. 3). The ionizer of the mass spectrometer lies within one flange of a 6 in. gate valve. The sniffer tube is 1.6 cm in diameter and 8.9 cm long and ends in a 150 μm orifice that admits gas from the reactor. The sniffer tube is mounted directly to the other gate valve flange and to a 2 $\frac{1}{8}$ in. diam flange attached to a welded bellows. When the sniffer is fully inserted it lies about 3.8 cm from the reactor axis. The distance between the sniffer tube orifice and the ionizer is 7.62 cm. The optical emission unit used is a Tracor-Northern TN6500, with a Polymicro Technologies 1148 fiber optic light pipe that transmits the signal from the Pyrex chamber window to the 0.5 m Czerny-Turner monochromator. There light passing through a 25 μm wide slit is reflected by one of three gratings (150, 300, and 600 lines/mm gratings) onto a 700 channel light-intensified photodiode array.

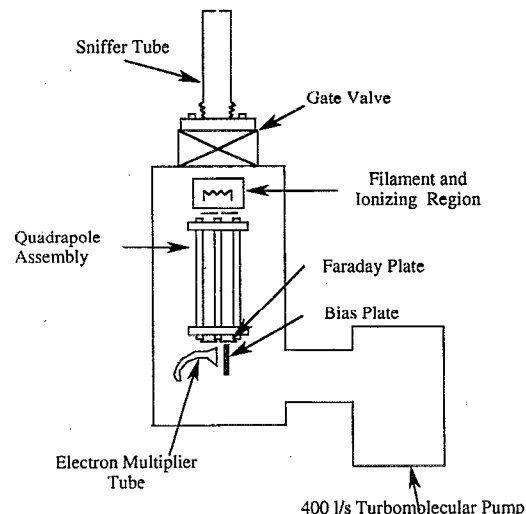


FIG. 3. Schematic diagram of Extrel C-50 quadrupole mass spectrometer inside of its pumping and sniffer tube enclosure.

There are two types of mass scan experiments performed on the afterglow of the plasma for this study, having either the ionizer of the mass spectrometer or the plasma as the sole ionization source. The first method involves turning off the ionizer and drawing ions from the plasma. Since only externally generated ions are detected, peak heights are *indicative* of the relative ion abundance in the reactor. The second method uses the mass spectrometer ionizer and a magnet placed adjacent to the throat of the sniffer tube to deflect externally generated ions into the sniffer tube walls so that they do not enter the mass spectrometer. This technique samples only neutral fragments, and the signal is mutually exclusive from the first method. It should be noted that the species detected by the mass spectrometer are those that traverse the sniffer tube. Because of the length of the tube, the mass spectrometer is most sensitive to species that have a low sticking probability. Therefore, the mass spectrometer is set up to examine the gas species that tend to be ground-state end products of gas-phase reactions.¹⁴

For analysis of SiH_4 interactions with the plasma, the following default operating conditions were observed: operating pressure of 300 mTorr, flow rates of 200 sccm He in the plasma tube, and 10 sccm 10% SiH_4 and 90% He mixture injected downstream through the gas dispersal ring. The 13.56 MHz power supply was used with the coil applicator and a default power of 50 W. All samples were grown at 250 $^\circ\text{C}$ substrate temperature. When H_2 was used, the flow rates were 200 sccm total flow with a composition of 0–40 sccm H_2 and the balance of He. In addition, for 0%, 10%, and 30% H_2 plasma feedstock composition, mass spectrometry signals were measured between 25 and 65 m/z to detect the presence of polysilane species.

III. RESULTS

A. Electrical characterization of the plasma

Electrical characterization of the plasma is necessary to understand plasma interaction mechanisms with SiH_4 .

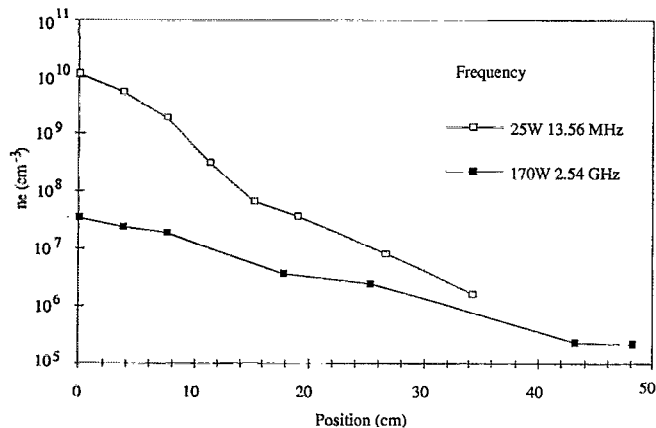


FIG. 4. Plot of n_e as a function of position for 13.56 MHz and 2.45 GHz excitation frequencies. 200 sccm He, 300 mTorr, 25 W at 13.56 MHz, and 170 W at 2.45 GHz.

Two plasma generation methods are compared, the 13.56 MHz and 2.45 GHz methods described above. Figure 4 shows the n_e with respect to distance from the opening of the plasma tube for 25 W at 13.56 MHz, and 170 W at 2.45 GHz. At the plasma tube opening, the electron density n_e for the 13.56 MHz discharge is roughly 2.5 orders of magnitude greater than that of the 2.45 GHz discharge, even though the applied power level is almost 7 times greater for the 2.45 GHz discharge. The decrease in n_e moving away from the plasma tube opening is approximately logarithmic for the 2.45 GHz curve, while the 13.56 MHz has a slight kink at about 10 cm, the position of the first set of gas dispersal rings. The 13.56 MHz n_e decreases by 4 orders of magnitude, and the 2.45 GHz n_e decreases by ~ 2.5 orders of magnitude at the far end of the chamber. Plotting the n_e as a function of power at various distances from the plasma tube as shown in Fig. 5 demonstrates that more than one charge generating mechanism is present in the 13.56 MHz discharge. As the Langmuir probe position increases the overall magnitude of n_e decreases, however the shape of the curve changes. Figure 5(a) shows that the n_e dependence follows a sublinear power function for positions less than 13.5 cm from the gas dispersal ring position, while positions greater than 13.5 cm show a superlinear dependence, as seen in Fig. 5(b). No corresponding plot was made for 2.45 GHz discharges due to the low signal intensity at all power levels.

Electron temperature as a function of position from the end of the plasma tube is shown in Fig. 6. Values for T_e range from 3.4 to 4.9 eV for the 13.56 MHz discharge, and from 1.5 to 3.0 eV for the 2.45 GHz discharge. However the most interesting feature of the 13.56 MHz curve is its shape at intermediate distances downstream from the plasma tube. The curve reaches a local minima at about 10 cm then a maxima at 13.5 cm, which coincides with the location of the first set of gas dispersal rings, before slowly decreasing at larger distances. The T_e for the 2.45 GHz discharge is about 30% lower than for the 13.56 MHz discharge at the mouth of the plasma tube. T_e for the 2.45 GHz discharge decreases linearly with respect to distance;

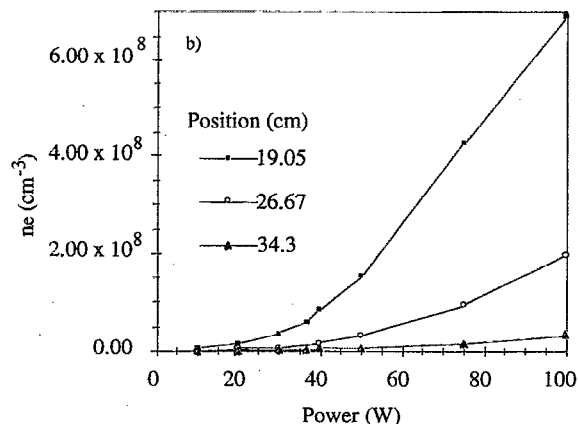
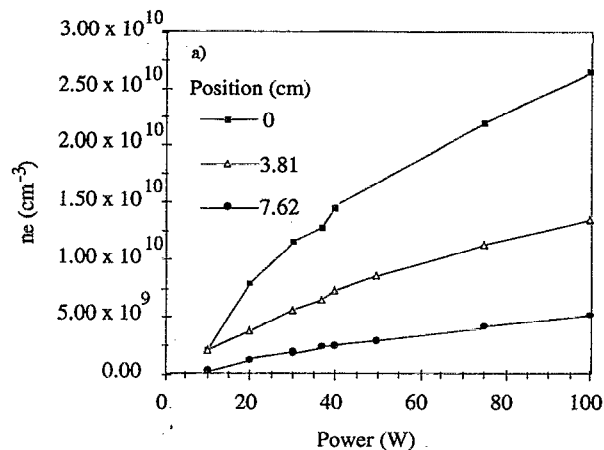


FIG. 5. Plot of n_e as a function of power at 13.56 MHz. 300 mTorr, 200 sccm He, (a) 0, 3.81 and 7.62 cm downstream, (b) 19.05, 26.67, and 34.3 cm downstream.

there is no increase in T_e near the first set of gas dispersal rings as detected for 13.56 MHz discharges. Figure 7 shows the relation of n_e at 34.3 cm from the mouth of the plasma tube related to the optical intensity of the 5015 Å (3^1P-2^1S) optical emission line for 200 sccm, 300 mTorr, 13.56 MHz plasmas. The purpose of this plot is to demonstrate the similarity of the behavior as a function of power of the relaxation of He optical states and n_e at distances far

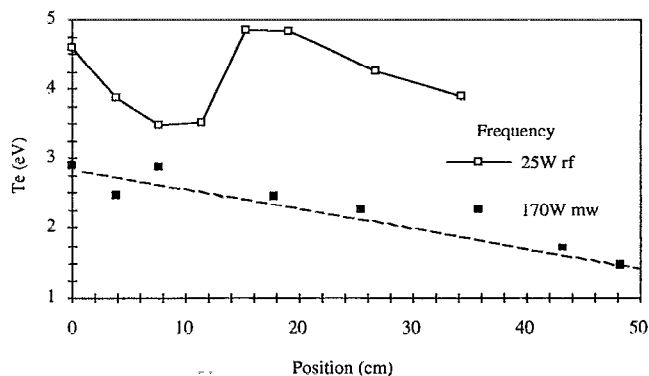


FIG. 6. Plot of T_e as a function of position for 13.56 MHz and 2.45 GHz excitation frequencies. 200 sccm He, 300 mTorr, 25 W at 13.56 MHz, and 170 W at 2.45 GHz.

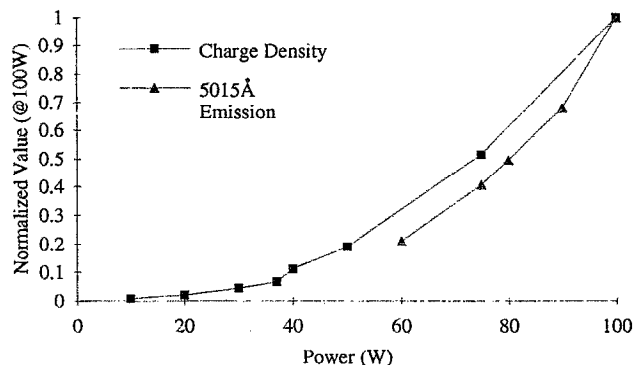


FIG. 7. Plot of n_e at 34.3 cm downstream, and 5015 Å light emission at 15.1 cm downstream as a function of power at 13.56 MHz. The data are normalized with respect to the 100 W data point.

from the end of the plasma tube. The normalized n_e curve has a slightly lesser exponent than the normalized optical emission curve, but in general the curves track one another.

B. Effects of the plasma on SiH₄

Figure 8 shows the intensities of two species that come from the injection of SiH₄ into the reactor, the 6561 Å ($3^2D-2^2P^0$ of H) and 4142 Å ($A^2\Delta-X^2\Pi$ of SiH) lines with respect to the SiH₄ source gas flow rate measured 2.45 cm downstream from the plasma tube.^{12,15} The signal intensities reach background levels above 10 sccm 10% SiH₄ and He in the downstream gas flow. It appears that the 6561 Å line reaches its intensity maximum at lower flow rates than the 4142 Å line. The intensity 5876 Å (3^3D-2^3P) and 5015 Å lines (not shown) decrease from 10⁵ to 6000 cps, a 17-fold drop, and 20500 to 2500 cps, an 8-fold drop, respectively.^{15,16} The ratio of 5876 Å/5015 Å declines from 5 to 2.5 for 0 and 25 sccm SiH₄, respectively.

Figures 9(a)–9(c) are mass spectrometer plots of reactor-generated ions between 20 and 320 m/z [Fig. 9(a) m/z 23–123, Fig. 9(b) m/z 123–243, and Fig. 9(c) m/z

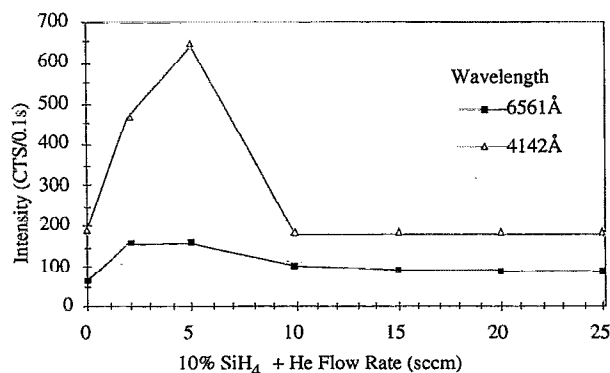


FIG. 8. 4142 and 6561 Å optical emission spectroscopy signals as a function of 10% SiH₄ + He flow rate injected downstream. 13.56 MHz discharge, 200 sccm He in the plasma tube, 300 mTorr, 50 W, sampling from the first viewport, intensifier gain 6.0, 0.1 s sampling time, 1000 cycles.

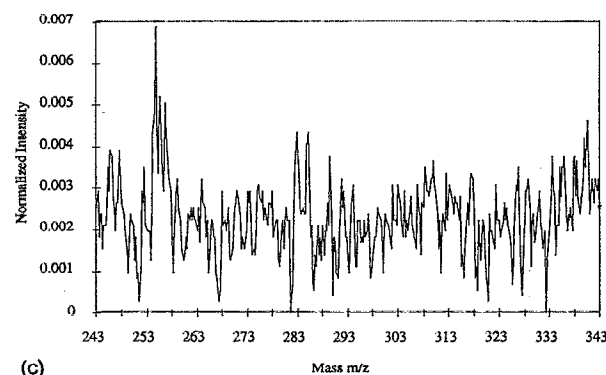
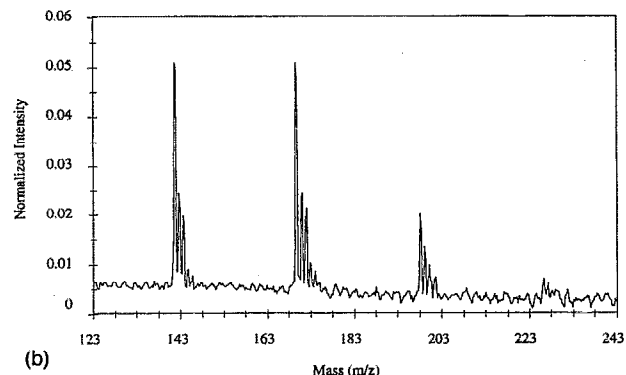
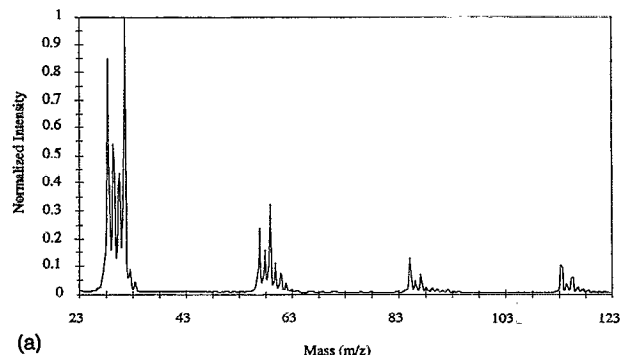


FIG. 9. (a) Mass 31 normalized mass spectra of multiple Si atom molecular ions, 23–123 m/z. 10 sccm 10% SiH₄ + He flow rate injected downstream, 13.56 MHz, 75 W, 200 sccm He in the plasma tube, 300 mTorr, mass spectrometer port No. 1, ionizer turned off. (b) Mass 31 normalized mass spectra of multiple Si atom molecular ions, 123–243 m/z. 10 sccm 10% SiH₄ + He flow rate injected downstream, 13.56 MHz, 75 W, 200 sccm He in the plasma tube, 300 mTorr, mass spectrometer port No. 1, ionizer turned off. (c) Mass 31 normalized mass spectra of multiple Si atom molecular ions, 243–343 m/z. 10 sccm 10% SiH₄ + He flow rate injected downstream, 13.56 MHz, 75 W, 200 sccm He in the plasma tube, 300 mTorr, mass spectrometer port No. 1, ionizer turned off.

243–363]. The chamber conditions are 300 mTorr pressure, 200 sccm He plasma feedstock gas, 10 sccm 10% SiH₄ and He, and 50 W power. Peak groups corresponding to Si_nH_x ($n=1$) starting at mass 28 m/z to peak groups at 308 m/z ($n=11$) are spaced at about 28 m/z intervals, where n is the number of Si atoms in the cluster. At 110 W, it is possible to detect peak groups up to 336 m/z ($n=12$). The average peak intensity declines as the number of silicon atoms in each peak group increase. Under certain conditions, it was observed that the peak group at 140 m/z

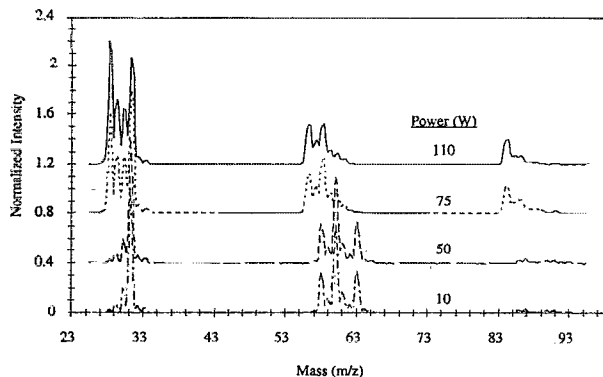


FIG. 10. Mass 31 normalized mass spectra of multiple Si atom molecular ions measured at different power levels, 23–98 m/z. 200 sccm He in the plasma tube, 10 sccm 10% $\text{SiH}_4 + \text{He}$, 300 mTorr, mass spectrometer port No. 1, ionizer turned off.

tends to be 33%–50% larger than the next lighter peak group at 112 m/z. This evidence of Si-cluster formation is similar to that of Ambacher *et al.*¹⁷ For peak groups where n ranges from 2 to 4, the number of peaks present is equal to $2n+4$, one peak extra than a normal silicon alkane analog chain number having $2n+3$ mass peaks.

Figure 10 shows the effect of plasma power upon the relative peak heights within each cluster peak group for m/z 23–98, demonstrating how the degree of hydrogenation changes as power increases. The conditions are 200 sccm He plasma feedstock, and 10 sccm 10% SiH_4 and 90% He mixture. The power levels are 10, 50, 75, and 110 W. The spectra are normalized with respect to the maximum intensity of mass 31, the three higher power spectra are offset from the base line for viewing clarity. For each peak group there is a tendency for the lower mass peaks to increase at higher power levels as the higher mass peaks decrease. At 10 W, there are peaks that exist at masses 63–65 that disappear at higher power levels (these correspond to Si-Cl groups attributed to residue from previous experiments). For the first peak group (28–33 m/z), the peak intensity of mass 28 increases with increasing power, until it becomes larger than mass 31 at 110 W.

In order to see at what rate SiH_4 is consumed as a function of power, Fig. 11 shows the 30 m/z signal intensity as a function of power normalized with respect to the 0 W signal level. The 30 m/z signal is a good measure of changes in SiH_4 concentration in the reactor, as the disilane peak intensity of 30 m/z is only 10% of its highest peak intensity at 60 m/z.¹⁸ It shows that the SiH_4 signal intensity drops logarithmically as a function of power for each sampled position. In addition when the plasma is ignited, the normalized SiH_4 signal intensities track each other for positions 2 and 3, but position 1 shows a 40% decrease. Figure 12 compares the effect of deposition rate and change in mass 30 signal loss as a function of plasma power. This demonstrates that the two phenomena are *not* directly related to one another. The mass 30 loss is calculated by normalizing the curve at position 2 in Fig. 11 with respect to the 0 W power intensity, and subtracting it from unity. The deposition rate shows an approximately linear

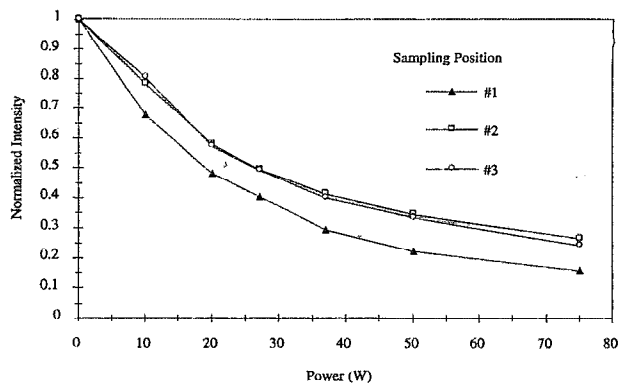


FIG. 11. Normalized 30 m/z mass spectrometry signal based upon neutral species as a function of power at all three sampling positions. 13.56 MHz discharge, 200 sccm He in the plasma tube, 10 sccm 10% $\text{SiH}_4 + \text{He}$, 300 mTorr. The three sampling positions are (1) 2.45 cm, (2) 13.35 cm, (3) 39.37 cm.

dependence on power. The signal loss percentage is defined as the amount of signal decrease for a mass signal between plasma off and plasma on conditions. The plot shows a saturation in the loss of the mass 30 signal of about 75% around 50 W.

Figure 13 is a series of mass spectrum plots from 25 to 95 m/z in which the plasma gas H_2 composition is 0%, 10%, and 30% for 200 sccm total gas flow (0, 18, and 58 sccm H_2 , respectively), 50 W 13.56 MHz power. The spectrometer is set up to detect only the fragments of neutral species. The peaks around 30 m/z are attributed to SiH_4 fragmentation and those centered around 60 m/z are attributed to disilane. Most noticeably, the disilane and trisilane peaks decrease with increasing H_2 content in the plasma gas. On the 10% H_2 spectrum, there is an increase in m/z 63 (also attributed to residual Si-Cl fragments), but the ratios of peak intensities of 0% and 30% H_2 are similar. However, there is no change in the peak ratios of the disilane associated peaks. The ratio of 30/31 goes from 0.5 at 0% H_2 to 1.3 at 30% H_2 , which is the ratio of m/z 30

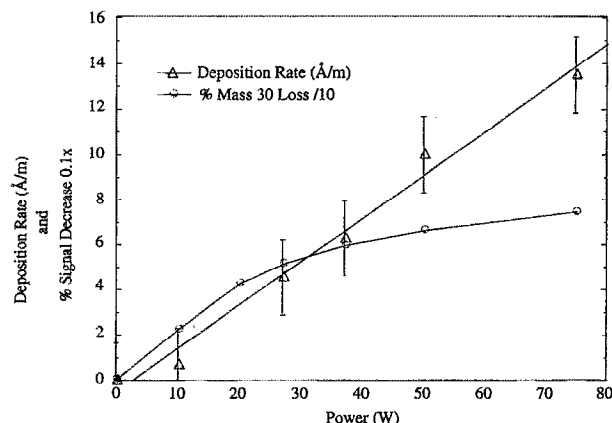


FIG. 12. Deposition rate and decrease in mass 30 loss as a function of power. 50 W, 13.56 MHz discharge, 300 mTorr, 200 sccm He in the plasma tube, and 10 sccm 10% $\text{SiH}_4 + \text{He}$ in the plasma tube.

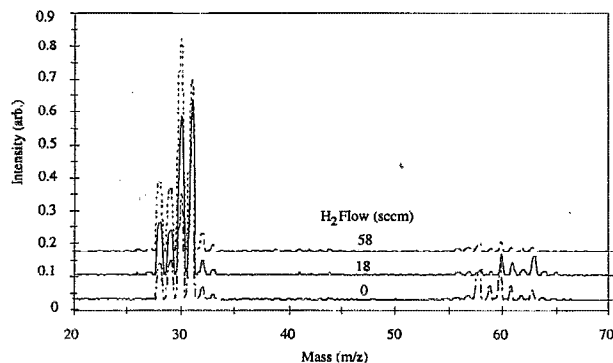


FIG. 13. Mass spectrum plots of a 10 sccm 10% $\text{SiH}_4 + \text{He}$, 300 mTorr, 50 W 13.56 MHz power, and a plasma gas of H_2 composition is 0%, 10%, and 30% and the remainder He for 200 sccm total gas flow.

to 31 for the SiH_4 cracking pattern. Mass 63 appears in this data, however it is due to the presence of chlorosilane residue in the reactor from a previous experiment. It should be noted that the 30% H_2 composition is sufficient to grow $\mu\text{-Si}$, while $\alpha\text{-Si:H}$ was grown at the other H_2 concentrations. Figure 14 is a plot of the disilane peak intensities as a function of the fraction of H_2 in the plasma feedstock gas. It shows that the m/z 58–60 intensities decrease by a factor of 3. The change in disilane peak mass intensities between 0 and 18 sccm H_2 show that mass 60 (Si_2H_4^+) decreases by at least 50%, while masses 58 and 59 (Si_2H_2^+ and Si_2H_3^+) decrease by 80%. This is evidence that as the hydrogen concentration in the plasma increases, the silane species produced become more highly hydrogenated.

C. Film deposition

Figure 15 is a plot of the deposition rate (from Fig. 12) for $\alpha\text{-Si:H}$ films at 14 cm downstream as a function of n_e (shown in Fig. 5) derived from double Langmuir probe measurements under similar operating conditions discussed above, except that there is no SiH_4 present. The relation follows a logarithmic behavior with a correlation coefficient of 0.954. Figure 16 demonstrates the relation

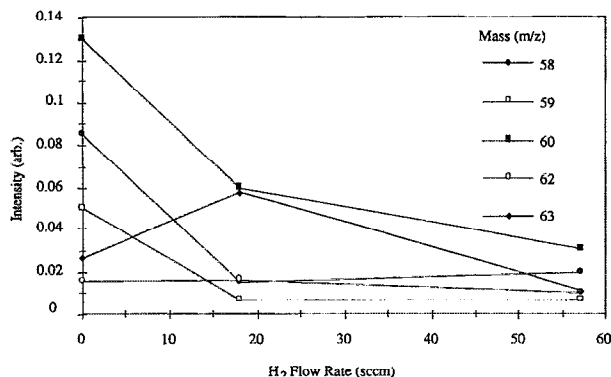


FIG. 14. Plot of the mass 58–63 m/z peak intensities as a function of the fraction of H_2 in of the plasma feedstock gas. Same conditions as in Fig. 13.

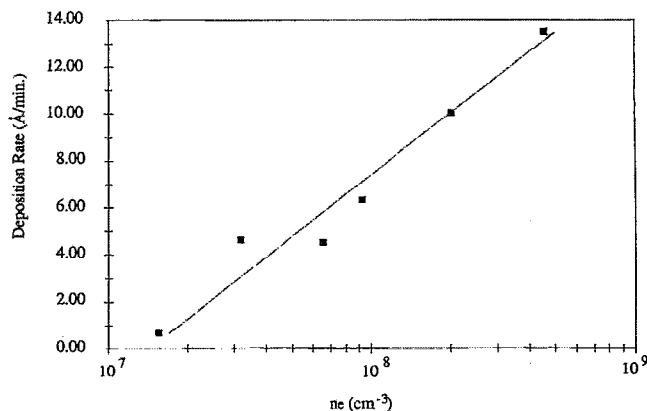


FIG. 15. $\alpha\text{-Si:H}$ deposition rate as a function of n_e . 13.56 MHz discharge, 300 mTorr, 200 sccm He in the plasma tube, 10 sccm 10% $\text{SiH}_4 + \text{He}$ injected downstream.

between the deposition rate of $\alpha\text{-Si:H}$ as a function of plasma tube to sample growth distance. The deposition rate decreases logarithmically as a function of substrate distance, with a correlation coefficient of 0.993. The logarithmic relation holds even for samples grown upstream from the SiH_4 injection point. A logarithmic regression fit of the curve gives the relation

$$d(x) = d_0 \exp\left(\frac{-x}{\lambda}\right), \quad (2)$$

where d is the deposition rate, x is the distance from the end of the plasma tube, d_0 is the deposition rate at the plasma tube, 233.3 Å/min, and λ is the characteristic length, 4.476 cm. Figure 17 shows the relation between deposition rate and SiH_4 gas flow, at 50 W power, and at a 13.4 cm distance between the plasma tube and the sample holder. The curve shows a deposition rate maxima around 10 sccm 10% SiH_4 and 90% He mixture, with a rapid drop toward lower flow rates and a gradual decrease at higher flow rates.

Infrared spectroscopy can be used to measure $[\text{H}]$ in thin films. The infrared spectrum of $\alpha\text{-Si:H}$ films has the following bands: the Si-H bending mode, $\text{SiH}(\text{b})$, at 630

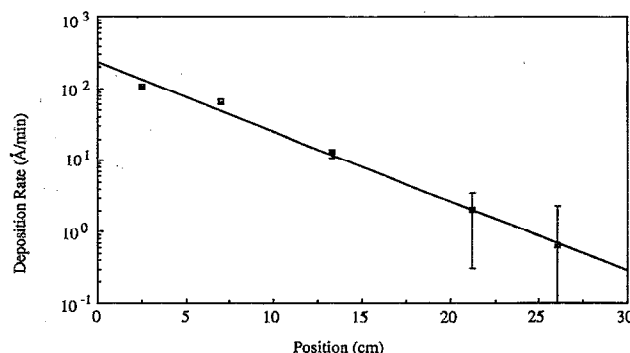


FIG. 16. Deposition rate as a function of the plasma tube opening film growth position distance. 200 sccm He in the plasma tube, 10 sccm 10% $\text{SiH}_4 + \text{He}$, 50 W, 13.56 MHz, 300 mTorr.

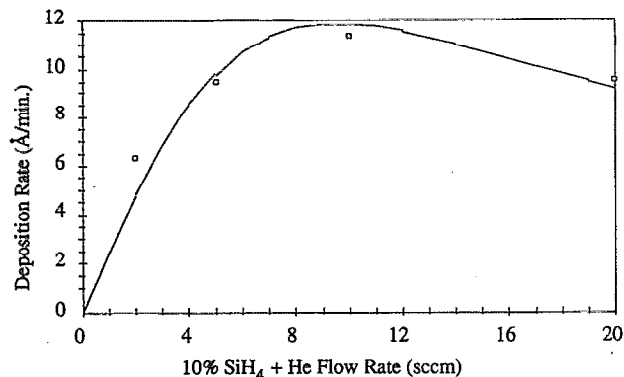


FIG. 17. α -Si:H deposition rate as a function of 10% SiH_4 + He flow rate. 13.56 MHz discharge, 50 W, 300 mTorr, 200 sccm He in the plasma tube, 13.3 cm downstream sample growth position.

cm^{-1} , and the SiH stretching mode, SiH(s), at 2000 cm^{-1} .¹⁹ For heavily hydrogenated films there is a SiH_2 stretching mode, Si-H₂(s), at 2100 cm^{-1} , and two chain-like SiH_2 scissors wagging modes, at SiH₂(w), at 850 and 900 cm^{-1} . While the data are not presented here, it is worth mentioning the behavior of the SiH content as a function of plasma power and He flow rate. In α -Si:H films, as a function of plasma power for samples grown 13.3 cm downstream from the plasma tube with the standard pressure and flow rates, the silicon-bound-hydrogen content abruptly increases in between 20 and 27 W, with a maximum hydrogen content of about $1.9 \times 10^{22} \text{ cm}^{-3}$, $\sim 27\%$. Above 27 W the hydrogen content remains relatively constant, but below 20 W there is a positive relation between power and hydrogen content. The hydrogen content [H] of α -Si:H films grown under the standard power and pressure conditions drops approximately linearly with increasing He flow rate. Figure 18 is a plot of the silicon dihydride group concentration [SiH_2] in various films as a function of the film deposition rate. The films were grown at different powers and growth positions, but at the standard flow rates and pressure stated above. The [SiH_2] increases linearly as a function of deposition rate, and has a linear regression correlation coefficient of 0.994.

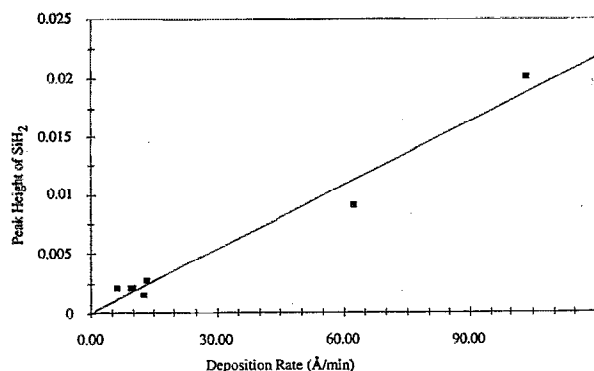


FIG. 18. Plots of the silicon dihydride group concentration in various films as a function of the films deposition rate.

IV. DISCUSSION

A. Charged species generation

The most significant observation of the electron temperature profile is that T_e increases between 8.5 and 15 cm for 13.56 MHz discharges (Fig. 6). The two electrodes are the rf coil and grounded chamber surfaces. This mode of coupling is consistent with the following observations: (1) the end of the coil that wraps around the plasma tube is not electrically connected to ground, yet it is still possible to ignite and sustain the plasma, (2) if the plasma is ignited, and then the end of the coil is grounded the plasma is extinguished, and (3) the ac impedance for coupling of the rf power to the plasma has capacitive reactance. At 13.56 MHz there is an electric field between the powered electrode and the grounded chamber that is able to generate charge in the reactor.

The lower n_e for the 2.45 GHz discharge compared to the 13.56 MHz discharge, shown in Fig. 4, seems to contradict direct PECVD results, but it is explained by the differences in coupling between the plasma and the chamber for these two plasma generation techniques.^{20,21} It has been established that n_e is significantly higher for the 2.45 GHz than for 13.56 MHz discharges.²²⁻²⁴ However for the 2.45 GHz remote PECVD technique, the excitation region is confined to the waveguide cavity, whereas for the 13.56 MHz discharge, the antenna and the interior of the reactor define the plasma generation region. This is a direct result of the different electrode configurations and discharge excitation frequencies used for initiating and maintaining the plasma discharge.⁴ Figure 4 shows that the 2.45 GHz discharge does not have the same degree of charge transport into the chamber, demonstrating that electric fields extending into the chamber are reduced to negligible levels compared with 13.56 MHz discharges. For the 2.45 GHz discharge, charge can only be transported into the chamber by thermal diffusion and gas flow. Thus it can be concluded that electrons are more likely to play a role in deposition reactions for the 13.56 MHz excitation than for the 2.45 GHz excitation, simply because of the electrode structures and excitation frequencies used to sustain the plasmas.

The plots of Fig. 5 show that there are two distinct mechanisms for creating charged species in the chamber from the fact that the function of n_e versus power changes only with distance. One mechanism must be electron impact ionization, since that is the mode by which the plasma is sustained. Charged species from electron impact ionization occur only in regions of significantly high electric fields, since these fields accelerate electrons to sufficient energy to cause ionization. Penning ionization, the formation of an ion/electron pair through metastable neutral collisions, is the other likely mechanism. The shape of the curves shown in Fig. 5(b) shows roughly the same behavior that is seen with light emission as a function of power. The behavior of light emission, a result of electronic relaxation of He excited atoms (He^*), is similar to n_e at positions further from the plasma tube, as shown in Fig. 7. Since the two phenomena behave similarly and He^* decay is the only method by which 5015 Å photons are formed in

this plasma, it is reasonable to say that they are dependent upon He^* concentration. For Penning ionization, the concentration of product is partially related to the square of $[\text{He}^*]$, since two metastables are required. The reaction rate for electron generation by the Penning ionization equation follows the form

$$\frac{dn_e}{dt} = k[\text{He}^*]^2, \quad (3)$$

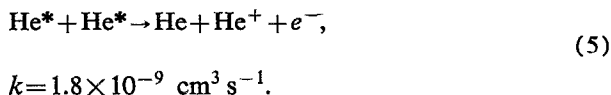
where k is the Penning ionization rate constant. The plots of Fig. 5 can be viewed as steady-state concentration plots of the products versus the reactants, because the n_e is the concentration of the product, and power is roughly proportional to the concentration of He^* , assuming voltage is constant and n_e is negligible relative to neutral density. At positions closer to the plasma generation region, for the 13.56 MHz discharge, the effect of Penning ionization becomes swamped by electric-field electron impact ionization.

In the 2.45 GHz discharge, the n_e in the reactor may be solely due to He^* Penning ionization. Since no electric field exists in the reactor to form ionizations through electron impact, only Penning ionization and unrecombined charge that diffuses from the plasma generation region are the sources of charge. It should be noted that the unrecombined charge diffusing from the plasma tube may be small, since at distances of 34.3 cm in the 13.56 MHz discharge charge appears to be primarily generated by Penning ionization, as shown by Figs. 5 and 7. The slightly smaller exponent of the n_e curve with respect to the 5015 Å curve in Fig. 7 may be due to a residual n_e component from field-induced electron impact ionization. Since the slope of the logarithm of n_e versus position for 2.45 GHz is constant, then it may be argued that it is dominated by Penning ionizations. Therefore, it is possible to describe the system with the continuity equation at steady state based upon Penning ionization

$$\frac{\partial n_e}{\partial t} = 0 = D_a \frac{\partial^2 n_e}{\partial x^2} - v \frac{\partial n_e}{\partial x} + k[\text{He}^*]^2 - k_r n_e^2, \quad (4)$$

where D_a is the ambipolar diffusion coefficient for charged particles, v is the thermal plug velocity of the flowing gas, and k_r is the electron/ion recombination rate. It is likely, from the argument above, that $\tau_r \gg k$.

The similarity of the absolute value of T_e for both 2.45 GHz and 13.56 MHz discharges, shown in Fig. 6, is somewhat puzzling. It would be expected that the microwave T_e be almost an order of magnitude lower.²⁵ One explanation is that a high energy tail of electrons exists in the discharge due to He Penning ionization reactions. Such reactions emit electrons with high energy compared with the bulk energy, 15–20 eV, versus 0.1–2 eV. The rate coefficient for Penning self-ionization is²⁶



The cross section for a room temperature gas is $4.5 \times 10^{-15} \text{ cm}^2$. A high energy electron tail in the distribution would shift T_e estimates of Langmuir probe data to higher values.

The double Langmuir probe data has shown that the plasma generation technique has an effect upon the power coupling to the discharge and that it has a strong effect of the charged species density in the reactor. The coaxial cable/13.56 MHz power application technique leads to a capacitively coupled discharge, while the TE_{01} waveguide/2.45 GHz power application technique leads to an inductively coupled discharge. This effect is a combination of the applied electromagnetic radiation and the method in which the radiation is brought into contact with the plasma generation region, i.e., the transmission mode. In addition, it shows that there are two distinguishable methods for generating charged species in the plasma, electron impact ionization and Penning ionization. Also, the primary mechanism for charge generation in the 2.45 GHz discharge in the reactor is from Penning ionizations. Finally, the similarity of T_e between the two generation methods may indicate the presence of very high energy electrons in the discharge, from the result of superelastic collision, or Penning ionization.

B. Silane interactions with the plasma

It is clear from Fig. 8 (SiH and H) that the plasma undergoes chemical changes upon the addition of SiH_4 . The most notable change is that intensities of all He lines decrease because energy is being diverted into the excitation of SiH_4 . The change in intensity ratio of the two He lines reflects a change in the excitation/relaxation pathways of He. The two methods that could account for this change are either a decrease in the generation rate of the excited species, or relaxation through a nonradiative process. It is likely that both processes occur at low SiH_4 concentrations—the reaction rate is limited by SiH_4 , which may limit He^* relaxation. At higher SiH_4 flow rates, energy is diverted to other channels such as SiH_4 fragmentation which may lower He^* formation. SiH_4 Penning excitation, which would require that He^*/SiH_4 cross sections be the He^* Penning self-ionization cross section, is one example of a nonradiative relaxation process. Yoshida *et al.* measured deexcitation reaction cross sections for He^* and SiH_4 to be on the order of 0.5 to $1 \times 10^{-14} \text{ cm}^2$ that roughly translates into a rate coefficient of $4.8 \times 10^{-10} \text{ cm}^3 \text{ s}^{-1}$ assuming room temperature gases. This value is about 25% the rate of Eq. (5).²⁷ It has been shown that the metastable density can approach the charged particles density in a discharge, so using n_e as an upper limit there may be as many as 10^{10} cm^{-3} He^* in portions of the reactor. The SiH_4 injected partial pressure is about 1.5 mTorr or $4.7 \times 10^{13} \text{ cm}^{-3}$. Therefore the relative populations of He^* and SiH_4 illustrate that this could be a deexcitation pathway for He^* . However due to the lack of deposition in the downstream portion of the main reactor where Penning processes dominate, it appears that Penning processes do not measurably contribute to film growth.

The ion mass spectrometer data presented in Fig. 9 demonstrate that the ionization source in the afterglow

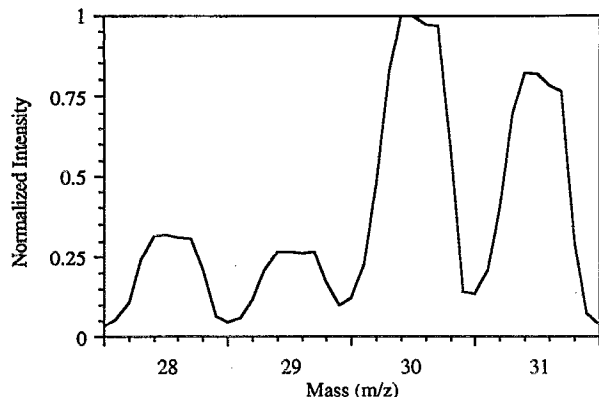


FIG. 19. Cracking pattern of silane. 70 eV electron beam.

discharge is not the same as single-collision electron impact ionization, because the plasma excitation pattern of SiH_4 species is much different from that of the neutral SiH_4 cracking pattern. The most important feature is that mass 31 is about 100% larger than mass 30. Mass 30 of the cracking pattern of neutral SiH_4 is normally 20% larger than mass 31 (Fig. 19). There are some physical differences between the ion generation of the mass spectrometer ionizer and the plasma. First, the electron energy is 70 eV in the mass spectrometer and is approximately monoenergetic, but the average electron energy in the reactor is less than 5 eV in the reactor. Furthermore, species in the mass spectrometer undergo at most one ionization event, while in the reactor, multiple collision events occur. The cracking pattern is not caused by the decomposition of polysilanes. A plot of electron impact ionization cross sections for SiH_4 shows that the cross section for SiH_2^+ is always greater than that for SiH_3^+ .²⁸ This means that the SiH_2^+ signal must be greater than the SiH_3^+ signal if electrons are the primary SiH_4 ionization source. Disilane and other polysilanes (polysilanes are defined as all Si-H compounds with at least 2 Si atoms) have been shown to produce a 2:1 ratio of SiH_3^+ to SiH_2^+ when fragmented by electrons.^{18,29} If 90% of the mass 28–31 signals were coming from polysilanes (the required concentration to obtain the 2:1 ratio), the disilane signal would be at least 5 times larger than the mass 28–31 signal.

The increase in applied power alters the fragmentation channels of the SiH_4 and polysilane ions produced in the plasma. As the power increases there is shift in the relative ratio of species produced, as seen in Fig. 10. Since the electron temperature remains effectively constant as a function of power, power is nominally proportional to n_e . The implication is that at higher n_e , SiH_4 products become less hydrogenated. The process of increased dehydrogenation is simply a result of a multicollision reaction sequence between excited species and the silicon-containing fragments.

It might be argued that SiH_2^+ could be selectively removed from the sampling gas as it travels the length of the sniffer tube due to wall collisions, since it has a greater sticking coefficient than SiH_3^+ . However the mass spec-

trometer only samples ions with line-of-sight trajectories, since the probability of electrical neutralization with the walls is unity. In addition, the low operating pressures within the sniffer tube ensures that gas-phase collisions are negligible. Thus sniffer tube wall collisions reduce all ion populations proportionally to their initial concentration. It is therefore necessary to consider multicollision mechanisms that contribute to SiH_4 ion formation.

What has been demonstrated is that polysilane fragments form as an effect of SiH_4 interactions with the discharge. The ion spectra produced by the plasma is not the same as seen from electron impact ionization. It has been argued that the process is either a multicollision one or nonelectron excitation. The fact that the interaction cross sections of He^*/SiH_4 and He^* Penning self-ionization are similar in size means that non-ion processes could also be considered along with charged species production when examining He^* relaxation. Because of the high pressure and slow plug velocity of the gas traversing the reactor, it must be considered likely that multicollision excitation processes occur in the reactor in measurable quantities.

C. Silane consumption pathways

Previous experiments have shown that α -Si:H films can be deposited by extracting active species from rf-excited He discharges in remote PECVD reactors.^{8,10} The microwave discharge glow region is maintained only within the portion of the plasma tube enclosed by the waveguide and its wings. It has been observed that α -Si:H films can be deposited from He discharges using rf excitation, but that these films cannot be deposited using microwave discharges. On the basis of Fig. 4, these results are consistent with the conclusions of previous studies.^{8,30} The density of charge particles, i.e., electrons, transported out the plasma excitation region of the rf plasma due to the electrode geometry is sufficiently high to promote measurable film deposition, while the density of electrons extracted from the microwave plasma is insufficient.

The mass spectrometer data, when compared with the deposition rate data, show that the injected SiH_4 is being converted into other nondepositing compounds when the plasma is ignited (see Figs. 11, 16, and 12.) Figure 11 shows that the decrease is substantially larger at position 1 compared with the other sampling positions. This is caused by the higher charge concentration in the vicinity permitting a higher reaction rate with SiH_4 . It is not, however, an effect of the lower SiH_4 concentration upstream of its injection point, since the curves are normalized to their plasma off condition for each position. The α -Si:H deposition reaction is not SiH_4 limited but rather charge limited, since the deposition rate is highest at positions closest to the plasma tube, as shown in Fig. 16. Figure 12 demonstrates that deposition rate and the mass spectrometer signals do not track as a function of power either, i.e., the mass 30 intensity is not a direct indication of the deposition rate. This independence demonstrates that there is another SiH_4 consumption channel.

Conversion into silicon thin films. Before examining the additional consumption channel, it is necessary to estimate the magnitude of the known pathways, such as film deposition. In order to determine the total fraction of SiH_4 consumed through deposition throughout the reactor, it is necessary to develop a procedure to determine the steady-state loss rate. One method is to estimate the equivalent flux required to sustain the measured deposition rate, however, as shown in Fig. 16, the deposition rate is not constant throughout the chamber. For example, at 50 W the signal intensity of the daughter species decreased by about 75% throughout the chamber and the measured deposition rate is 103 Å/min at 2.5 cm downstream. The flux of SiH_4 injected into the reactor is $4.08 \times 10^{17} \text{ s}^{-1}$. Assuming that the density of incorporated Si is $5.00 \times 10^{22} \text{ cm}^{-3}$, then the

maximum incorporation volume rate is $8.17 \times 10^{-6} \text{ cm}^3 \text{ s}^{-1}$. If this is material deposited evenly across the entire surface area of the reactor, then the deposition rate would be 17.6 Å/min.

Figure 16 can be used to estimate the average deposition rate of material throughout the reactor. The flux density of consumed Si_nH_x species in the chamber can be simply stated as the average incorporated flux density in the chamber, $\langle j_{\text{inc}} \rangle \equiv \langle d \rangle \rho$, where $\langle d \rangle$ is the spatially averaged steady-state deposition rate, and ρ is the atomic density of Si. Assuming that the deposition rate is a function of the linear distance from a surface point in the reactor and the center of the opening of the plasma tube, the average deposition rate is

$$\langle d \rangle = \frac{\int_0^{z_1} d 2\pi r_c (\sqrt{z^2 + r_c^2}) dz + \int_{r_1}^{r_c} 2\pi r d(r) dr + d(z_1) \pi r_c^2}{2\pi z_1 r_c + 2\pi r_c^2}, \quad (6)$$

where z_1 is the chamber length, r_1 is the plasma tube radius, and r_c is the chamber radius. This method accounts for the fact that the samples used for measuring the deposition rate were not at the same position as the walls of the reactor. This approximation is required because a straight correlation of distance from the end of the plasma tube and the sample growth position implicitly assumes that the reactor diameter is the same as the sample diameter. Because the deposition rate at the far end of the reactor z_1 is small (0.007% of the near-end deposition rate) the third term of the numerator is neglected. Integrating the second term of the numerator yields

$$2\pi \int_{r_1}^{r_c} r d_0 \exp\left(\frac{-r}{\lambda}\right) dr = 2\pi d_0 \lambda^2 \left[\exp\left(\frac{-r_c}{\lambda}\right) \left(\frac{-r_c}{\lambda} - 1\right) - \left[\exp\left(\frac{-r_1}{\lambda}\right) \left(\frac{-r_1}{\lambda} - 1\right) \right] \right]. \quad (7)$$

Solving Eq. (6) for $d(z)$ from Eq. (2), where d_0 is 233 Å/min, r_c is 7.62 cm, λ is 4.476 cm, and z_1 is 43 cm, r_1 is 1.91 cm plasma tube radius; numerically integrating the first term of the numerator by the method of Gaussian quadrature; and dividing the entire numerator by a surface area of 2788 cm², yields $\langle d \rangle = 11.3 \text{ Å/min}$ [depositing flux of $2.64 \times 10^{17} \text{ s}^{-1}$]. Given that the injected SiH_4 flux is $4.46 \times 10^{17} \text{ s}^{-1}$, the conversion of SiH_4 into solid thin film material in this remote PECVD reactor is about 65%. This simple estimate does not account for the spatial concentration gradient of SiH_4 and n_e in the reactor, nor does it account for nonuniformity caused by shadowing and the extra surface area of the sample holder, ports, and gas dispersal rings. The effect of elevated substrate temperature

should not make a major correction to the deposition rate, since it is not normally measurable for temperatures less than 300 °C.^{11,31}

Polysilane formation. It has been shown that virtually all of the SiH_4 injected into the reactor is converted into a solid product. Furthermore evidence has been presented that shows that measurable quantities of SiH_4 are converted into polysilanes. The question prevails of the magnitude of this gas-phase polymerization to determine its significance to the deposition reactions. By examining the mass spectra of the polysilanes it is possible to find the limits of relative concentration of polysilanes to the injected silane signal. Polysilane species can contain a large fraction of Si atoms while having small signal levels compared to SiH_4 . There is the linear relation between each particle for species Si_nH_x detected (the number of Si atoms n .) A corollary to that is n is the number of SiH_4 molecules consumed to manufacture each Si_nH_x . Assuming that the ionization cross sections are similar for the polysilanes as they are for SiH_4 , a mass spectrometer signal for a Si_4H_x species that is 4 times smaller than the equivalent SiH_4 signal, represents the same number of Si atoms. Therefore, the average branching ratio would be the inverse of the number of possible H bonds on the material + 1, or $2n + 3$, where n is the number of Si groups in the chain. The signal defining the number of Si atoms in each unit of the signal is

$$\text{No. of Si atoms} = \frac{\text{signal} \times \text{No. of Si atoms in chain}}{\text{average branching ratio}} \quad (8)$$

or

$$\text{No. of Si atoms} = \text{signal} \times n(2n + 3). \quad (9)$$

For example, for a peak group Si_6H_x , the average signal intensity for the peak group would be multiplied by a factor of 90 to account for all of the SiH_4 molecules consumed. The following example illustrates the determination of the ratio of Si within the polysilane species to the Si within the SiH_4 source. Figure 9 shows the mass spectrum ion signal normalized with respect to mass 31. The spectrum shows the relative ion fluxes for all Si-containing species generated in the chamber from neutral precursors. The relative size of the Si_nH_x species is found by adding all of the terms for all of the Si_nH_x peaks for the equation. For all of the peaks for peak groups larger than SiH_4 itself, using the method described previously, the total count is 7.2, while the SiH_4 peaks yield a count of 2.8. This indicates that about 2.6 times more Si atoms reside in the multi-Si ion clusters than in the SiH_4 when the plasma is on. Furthermore since the externally generated ions are indicative of the concentration of neutral particles in the plasma, it may be said that $\sim 60\%$ of the gas-phase Si atoms reside in polysilane neutral molecules and fragments.

The gas signal mass balance between SiH_4 and polysilanes balances when comparing Fig. 11 and the mass spectrometer signal levels of polysilane and SiH_4 . As shown in Fig. 11 the mass 30 signal, which represents SiH_4 , drops by about 75% when the plasma is at power levels similar to the 65% of Si that is deposited. This demonstrates that most of the loss of SiH_4 from the gas phase is converted into solid material. Even though there is considerable error in the total film production rate estimate, the fact that not all of the consumed SiH_4 is converted into a solid product implies that some of the polysilane species are pumped from the reactor. Therefore it shows that polysilane species must be accounted for in remote PECVD processes utilizing SiH_4 .

The formation of polysilanes in direct glow discharges by radical insertion reactions with SiH_4 has been well documented.³²⁻³⁵ Kushner has modeled the production of these species in PECVD systems for α -Si:H growth and discussed that (1) polysilanes form through substitution reactions of radical and ion silane species, and (2) the observed Si_3H_x anomalous concentration is due to the presence of an activation energy barrier to the formation of longer chains.³² These modeling results are supported by the work of Weakliem *et al.* in that these species were produced in glow discharges.³³ It is reasonable to therefore extrapolate the notion that similar processes are possible in the remote PECVD, since electrons are drawn into the reactor, and large dimension volumes (several centimeters) exist.

Earlier work on α -Si:H production by remote PECVD did not detect polysilanes in a 5.1 cm diameter reactor.³⁰ There are four reasons that they were not detected in earlier remote PECVD experiments. First of all, it is possible that the narrower reactor inhibited measurable polysilane formation. SiH_2 fragments are quite reactive, since they have the ability to insert themselves in silanes.³²⁻³⁶ Therefore they react as readily on a silicon surface as with another Si-containing species in the gas phase. If a SiH_2 molecular fragment collides with another Si-containing

molecule before encountering a surface, the molecular fragment reacts with the it, thus removing it from the deposition reaction as a single SiH_4 molecular fragment. Since the volume/surface area ratio decreases with diameter, a 5.1 cm diam reactor has a higher SiH_2 insertion rate into the film than the 15 cm diam reactor. The second possibility is that experiments in the 5.1 cm reactor used SiH_4 diluted in Ar instead of He. Argon competes with SiH_4 for reactions with excited He, thus limiting SiH_4 molecular fragment production. Thirdly the narrower reactor diameter leads to a gas plug velocity that is an order of magnitude higher. When the plug velocity increases then the degree of reaction completion of any point along that reactor drops, though it is admittedly small when the reaction rate constants are orders of magnitude larger than the plug velocity. All three factors inhibit the production of the polysilane molecules. The fourth reason is that most of the detection of SiH_4 in remote PECVD discharges utilized the mass spectrometer ionizer. This method of detection can fragment polysilanes into smaller species and swamp the chamber-generated ion signal with the mass spectrometer-produced ion signal.

Similar geometric arguments may be proposed for direct PECVD reactors. Until recently, most direct PECVD studies have not been able to detect polysilanes. Most parallel plate reactors have a 2–5 cm spacing between the electrode plates. This spacing may be too small to permit measurable formation rates of polysilanes due to SiH_2 consumption by surface sites, because of the proximity of the surface to the generation of SiH_2 . Polysilane species have recently been reported in direct PECVD discharges, in which Si_3H_x species also showed higher than expected concentrations.¹⁷

Thin film conversion efficiencies. By curve fitting the appropriate functions from Figs. 15 and 17, it is possible to empirically determine the relative efficiencies of electrons and SiH_4 , respectively, for growing α -Si:H films. By converting the deposition rate and steady-state SiH_4 partial pressure as determined from the mass spectrometer data, and using the n_e estimate from the Langmuir probe data, it is possible to empirically determine the reaction orders with respect to each reactant. Equation (10) is the logarithmic regression fit for the deposition rate as a function of n_e . The prefactor for Eq. (10), 3.79 Å/min , translates into a sticking Si precursor flux density of $3.16 \times 10^{13} \text{ cm}^{-2} \text{ s}^{-1}$ assuming a unity sticking coefficient,

$$d = 8.73 \text{ Å/min} \log_{10} \left(\frac{n_e}{1.42 \times 10^7 \text{ cm}^{-3}} \right) \quad (10)$$

(for comparison, the SiH_4 flux density in the downstream sections of the chamber without a discharge is $5.45 \times 10^{17} \text{ cm}^{-2} \text{ s}^{-1}$). The Si precursor concentration term can be used instead of the deposition rate to find the number of source gas molecules consumed for a given n_e value. For example, for 10 sccm SiH_4 flow rate, if the n_e in the vicinity of the sample is 10^9 cm^{-3} , the flux density of the incorporated SiH_4 precursor is $1.34 \times 10^{14} \text{ cm}^{-2} \text{ s}^{-1}$, or a deposition rate of 16 Å/min .

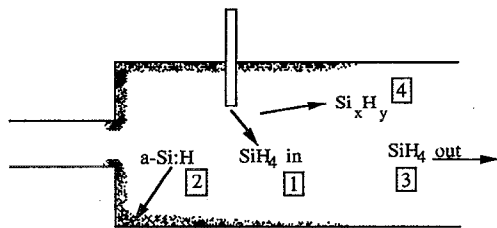


FIG. 20. Schematic diagram of Si mass balance between injected silane and Si film growth.

The SiH_4 efficiency relation is higher than first order due to the parallel consumption of SiH_4 into larger polysilane. The equation has the form

$$d = \kappa \frac{p_{\text{SiH}_4}}{1 + \kappa' p_{\text{SiH}_4}^2}, \quad (11)$$

where κ and κ' are fitting parameters for the equation, and p_{SiH_4} is the partial pressure of SiH_4 , see Fig. 17. This equation accounts for the increasing likelihood of Si cluster-forming reactions, at the expense of film deposition. The SiH_4 partial pressure may be determined by multiplying the percentage decrease in the mass 30 signal between discharge on and off levels by the SiH_4 partial pressure with discharge off. Fitting Fig. 17 to this equation yields $\kappa = 2.5 \text{ Å min}^{-1} \text{ sccm}^{-1}$, and $\kappa' = 10^{-2} \text{ sccm}^{-2}$.

D. Mass balance model

There are several outcomes of the interaction of SiH_4 molecules with a discharge afterglow in the remote PECVD reactor. The first step in understanding the process is to enumerate these channels, which are shown in Fig. 20. The overall mass balance of the equation is given in Eq. (13), where (1) is the injected SiH_4 flow rate, (2) is the film growth rate, (3) is the unconsumed SiH_4 flow rate, and (4) is the flow rate of Si_xH_y clusters

$$(1) = (2) + (3) + (4) \quad (12)$$

or

$$\text{SiH}_4(\text{in}) = \text{Film} + \text{SiH}_4(\text{out}) + \text{Si}_x\text{H}_y(\text{out}). \quad (13)$$

Equation (13) is different from previous discussions of the remote PECVD process in that it includes a term for the polysilane reaction product. The significance of the Si_xH_y (polysilane) term is that these species can contribute to the deposition of $a\text{-Si:H}$. Larger cluster polysilanes (say $\text{Si}_n > 4$) may inhibit the ability to grow crystalline materials through lowered surface mobility of silicon and the creation of defect sites by clusters. The model presented here reflects the presence of these polysilane species.

As shown above, the polysilane channel is large enough that it must be added to the mass balance. Even though ground-state neutral disilane species are about as reactive as ground-state neutral SiH_4 , the polysilanes are subjected to the same excitation processes as SiH_4 . It is reasonable to argue that if polysilane can be so excited,

they can be as reactive as decomposed monosilane fragments. Since they exist in a similar concentration as SiH_4 , it is reasonable to conclude that they contribute to $a\text{-Si:H}$ film growth for remote PECVD. Therefore it is necessary to include the contributions of polysilane in the mass balance

Film Mass Balance:

$$\text{Film} = \text{SiH}_4(\text{Film}) + \text{Si}_x\text{H}_y(\text{Film}), \quad (14)$$

Cluster Mass Balance:

$$\text{Si}_x\text{H}_y = \text{Si}_x\text{H}_y(\text{Film}) + \text{Si}_x\text{H}_y(\text{out}), \quad (15)$$

Silane Mass Balance:

$$\text{SiH}_4(\text{in}) = \text{Si}_x\text{H}_y + \text{SiH}_4(\text{Film}) + \text{SiH}_4(\text{out}). \quad (16)$$

Equation (14) shows the contribution of the two silicon sources, Eq. (15) shows the balance of polysilane formation and consumption, while Eq. (16) shows the sources and sinks of SiH_4 . To confirm the validity of Eq. (13) it is necessary only to add the contributions of each consumption channel to the mass balance. Even though the net result is the same, it shows polysilanes need to be included when performing the mass balance on $a\text{-Si:H}$ deposition.

The calculation of the fraction of SiH_4 consumed in thin films and polysilane production can be used in Eqs. (12) and (13). The amount of material that is converted into a solid product (Film) has been calculated at 65% of the total injected SiH_4 [$\text{SiH}_4(\text{in})$] which is 100%. From Fig. 11, it has been shown that the SiH_4 level drops to 25% when the plasma is ignited. This value appears constant at both positions No. 2 and No. 3 which implies that 25% of the SiH_4 is consumed, especially since there is little reaction at position No. 3. If the assumption that the plasma produces silane and polysilane ions in proportion to their neutral population, then the exhausted polysilane fraction [$\text{Si}_x\text{H}_y(\text{out})$] is $\sim 65\%$. When these three terms are added together they obviously exceed 100%. The sources of error in the estimates of the actual fraction of polysilanes produced and exhausted SiH_4 , must be attributed to different excitation cross sections for the different species. In any case, the polysilanes must contribute to growth since they are chemically similar to SiH_4 .

E. Film growth

The reactive SiH_4 species that are formed have different reaction rates in the gas phase and on the surface of the growing films.^{37,38} Changes in the concentration of hydrogen in $a\text{-Si:H}$ films highlight the difference in the reaction rates. The abrupt increase of silicon-bound hydrogen concentration [SiH] as a function of power shows a discontinuous increase that may be argued along the lines of multiple deposition species competing in film growth by varying concentrations.

Tanaka and Matsuda proposed that the deposition mechanism governing $a\text{-Si:H}$ film morphology is based on the surface mobility of reactive SiH_4 species, and that hydrogen termination of the network permits increased mobility for certain molecular fragments.^{37,38} They theorized

that SiH_3 incorporation requires a hydrogen-free surface site, while the SiH_2 molecular fragment can abstract hydrogen and insert itself. They further showed that in the gas phase, the SiH_3 molecular fragment has a longer lifetime compared with other SiH_4 molecular fragments because of its relative unreactivity with other SiH_4 species, thus it can diffuse farther. SiH_2 , on the other hand, is likely to react with the first Si-containing particle it encounters whether it is on the surface or in the gas phase. Therefore SiH_2 needs to be generated in the vicinity of the growing film to be incorporated.

This theory explains the change in $[\text{SiH}]$ as a function of power, as mentioned in Sec. III C. At lower power levels, the survival rate of SiH_2 to the substrate is too low to be significant hence deposition is driven by SiH_3 . However, once the plasma intensity is great enough to generate SiH_2 in the vicinity of the growing film, the surface state of the film is no longer an issue to film growth. Network propagation no longer requires hydrogen removal, so the hydrogen incorporation rate increases. It has been shown in Fig. 10 that the power increases the amount of less hydrogenated silanes, which are a source of surface-insensitive deposition species. The incorporation of SiH_2 groups in the films appears to be a function of surface reaction kinetics since it is only dependent upon the deposition rate at a constant temperature, but independent of power and gas concentrations, as shown in Fig. 18. One explanation is that SiH_2 has a finite lifetime on the surface. The deposition rate is proportional to an encapsulation rate of the SiH_2 , so higher deposition rates lead to higher SiH_2 concentrations. Knowledge of the infrared correlation constant for $[\text{SiH}_2]$ in $\alpha\text{-Si:H}$ would determine the concentration of SiH_2 and make it possible to determine the encapsulation rate coefficient.

Growth of microcrystalline silicon in remote PECVD has been shown to require H_2 injected into the reactor. There are three possible mechanisms by which it affects the growth of microcrystalline silicon, suppression of formation of low-mobility deposition molecular fragments, hydrogen termination of the growing crystal surface, and etching of off-crystal-site silicon atoms. These latter two mechanisms have been discussed in the literature and relate to the surface chemistry of the growing film. The first mechanism, however, would require a change in the gas-phase chemistry of the process. There are two general methods by which hydrogen suppresses $\alpha\text{-Si:H}$ precursors. Such suppression can be expected as the system strives to achieve chemical equilibrium between SiH_4 , SiH_x ($0 < x < 3$) and hydrogen. In the first mechanism as the H_2 concentration increases, the gas-phase chemical equilibrium of the SiH_4/H_2 system shifts towards the SiH_4 species with higher degrees of hydrogenation (Le Chatelier's Principle).^{32,39} The second mechanism involves the presence of H_2 in the afterglow (58:1 H_2/SiH_4 ratio) as shown by the decrease in disilane peaks in the mass spectra. Hydrogen dissipates the discharge energy through either vibrational excitation, Penning ionization with He^* or fragmentation from electron impact. This hydrogen shielding can lower the SiH_4 fragmentation and ionization rates.

The most notable feature in Figs. 13 and 14 is the decrease in the disilane signal with increasing H_2 concentration. There are two explanations for the relationship between the disilane signal level and $\mu\text{c-Si}$ film growth. First, it is possible that disilane contributes to $\alpha\text{-Si:H}$ growth, and that lowering its concentration permits $\mu\text{c-Si}$ growth. While neutral disilane is not reactive, molecular fragments of disilane and polysilanes are. Large polysilane groups will have a relatively lower surface mobility than monosilane groups, and will act as nucleation sites, so polysilane incorporation will be more likely to lead to $\alpha\text{-Si:H}$ network propagation. Reducing the polysilane concentration reduces the $\alpha\text{-Si:H}$ growth reactions. The second explanation is that the disilane concentration is merely an indication of the SiH_2 concentration. SiH_2 incorporates itself into existing silicon networks through insertion reactions forming either multiple silicon atom molecules or silicon films. Such SiH_2 insertion leads to $\alpha\text{-Si:H}$ formation. If the disilane signal decreases it indicates that the SiH_2 concentration has also fallen.

The etching of silicon surfaces by hydrogen has been demonstrated in Fig. 13. It shows that mass 63 increases up to an intensity that is almost as great as mass 60 at 18 sccm H_2 , but it is not identifiable as a Si_2H_6 peak. The peak can be attributed to an experimental artifact, SiCl . SiCl removed from the chamber walls is a remnant of SiH_2Cl_2 decomposition in the chamber prior to this experiment. Monochlorosilanes have masses ranging from 63 to 67, considering ^{35}Cl and ^{37}Cl , so there is no signal overlap with disilane. It is unlikely that Cl is merely removed from the reactor walls and reacts with gas-phase SiH_4 , because of the absence of significant Cl and HCl peaks in the spectra. At 0 sccm H_2 , the mass 63 peak indicates a lower rate of monochlorosilane removal from the walls, even though the concentration of these species is higher, since the spectrum was collected before the 18 sccm spectrum. The increase in the mass 63 intensity upon addition of H_2 shows that H_2 is stripping SiCl from the reactor walls. The drop in mass 63 at higher H_2 flow rates is merely caused by depletion of chlorosilanes from the walls, since the 58 sccm H_2 scan was made after the 18 sccm H_2 mass scan. This indicates that addition of H_2 enhances etching of the silicon surfaces.

V. CONCLUSIONS

It has been shown that the plasma generation technique has an effect upon the power coupling to the discharge and that it has a strong effect of the charged species density in the reactor, in that the 13.56 MHz technique leads to a capacitively coupled discharge, while the 2.45 GHz technique leads to an inductively coupled discharge. There are two distinguishable methods for generating charged species in the plasma, electron impact ionization and another mechanism, Penning ionization. The primary mechanism for charge generation in the reactor using 2.45 GHz discharges is Penning ionization. In addition, it has been shown, that while Penning ionization is a measurable phenomenon, as an excitation mechanism its rate is too low to significantly affect $\alpha\text{-Si:H}$ deposition.

What has been demonstrated is that SiH_4 is affected by the discharge, by forming polysilanes. In light of the fact that two charge production mechanisms are detectable in this process, it can be stated that $\alpha\text{-Si:H}$ growth is stimulated by field-accelerated electron impact of SiH_4 in remote PECVD processes. It is possible to produce polysilane species from a He/SiH_4 afterglow in a remote PECVD system. What has also been shown is that these polysilanes account for a significant fraction of the gas-phase SiH_4 conversion in the reactor. A simple model incorporating the effect of polysilane presence has been presented. In fact, due to the chemical similarity of these polysilanes and their concentration relative to SiH_4 , they should be considered in models of silicon thin-film growth in remote PECVD.

Hydrogen has been shown to reduce the presence of polysilane species in the plasma for conditions that are conducive to $\mu\text{c-Si}$ growth. In addition, the silane species exhibit a higher degree of hydrogenation at the hydrogen flow rate is increased. This increased hydrogenation is likely to inhibit the production of SiH_2 species. The implication is that hydrogen may affect the $\mu\text{c-Si}$ process in the gas phase as well as through possible surface reactions. The effect of hydrogen on silicon surfaces was made apparent by the liberation of chlorine-containing silane species upon the addition of hydrogen to the plasma. In discharges without hydrogen present, the presence of SiH_2 in the films appears to be a purely surface kinetics phenomena, since it is only dependent upon the deposition rate for a constant temperature. In addition, it was demonstrated that H_2 can etch silicon surfaces by the increased removal rate of monochlorosilanes from film surfaces when hydrogen is present in the afterglow.

ACKNOWLEDGMENTS

The authors would like to thank Dr. G. Lucovsky for the use of his facilities for performing this work and his guidance during the research. In addition, they would like to thank the Advanced Electronic Materials Processing Engineering Research Center, and the North Carolina Semiconductor Center of Excellence for providing funding for this research. G. Powell, would also like to thank Dr. M. Paesler and the Research Experience for Undergraduates Program of the National Science Foundation. They would also like to thank Dr. T. Yasuda for his useful discussions and suggestions.

¹ J. A. Theil, G. Lucovsky, S. V. Hattangady, G. G. Fountain, and R. J. Markunas, *Mater. Res. Soc. Symp. Proc.* **260**, 601 (1991).

² G. Lucovsky, G. N. Parsons, C. Wang, B. N. Davidson, and D. V. Tsu, *Solar Cells* **27**, 121 (1989).

³ T. Hsu, L. Breaux, B. Anthony, S. Banerjee, and A. Tasch, *J. Electron. Mater.* **19** (1990).

⁴ J. A. Theil, S. V. Hattangady, and G. Lucovsky, *J. Vac. Sci. Technol. A* **10**, 719 (1992).

⁵ D. V. Tsu, S. S. Kim, J. A. Theil, C. Wang, and G. Lucovsky, *J. Vac. Sci. Technol. A* **8**, 1430 (1990).

⁶ J. A. Theil, D. V. Tsu, and G. Lucovsky, *J. Electron. Mater.* **19**, 209 (1989).

⁷ D. V. Tsu, G. N. Parsons, and G. Lucovsky, *J. Vac. Sci. Technol. A* **6**, 1849 (1988).

⁸ D. V. Tsu, G. Lucovsky, and M. W. Watkins, *Mater. Res. Soc. Symp. Proc.* **131**, 289 (1988).

⁹ *Thin Film Processes II*, edited by J. L. Vossen and W. Kern (Academic, San Diego, 1991), pp. 529–531.

¹⁰ A. Matsuda and K. Tanaka, *Thin Solid Films* **92**, 171 (1982).

¹¹ G. N. Parsons, Doctoral Dissertation, North Carolina State University, Raleigh; 1989.

¹² Richard Myers (private communication, 1991).

¹³ A. Matsuda and K. Tanaka, *Thin Solid Films* **92**, 171 (1982).

¹⁴ J. A. Theil, Doctoral Dissertation, North Carolina State University, Raleigh, 1992.

¹⁵ W. L. Wiese and G. A. Martin, NBS Monograph #68: Transition Probabilities, US Gov't. Doc. C13.48 68, 359.

¹⁶ G. Herzberg, *Atomic Spectra and Atomic Structure* (Dover, New York, 1944), pp. 24, 65.

¹⁷ O. Ambacher, W. Rieger, K. Schopper, and S. Veprek, *J. Electrochem. Soc.* **140**, 1935 (1993).

¹⁸ P. Potzinger and F. W. Lampe, *J. Phys. Chem.* **73**, 3912 (1969).

¹⁹ M. H. Brodsky, M. Cardona, and J. J. Cuomo, *Phys. Rev. B* **16**, 3556 (1977).

²⁰ D. Landheer, N. G. Skinner, T. E. Jackman, D. A. Thompson, J. G. Simmons, D. V. Stevanovic, and D. Khatmian, *J. Vac. Sci. Technol. A* **9**, 2594 (1991).

²¹ B. Anthony, T. Hsu, R. Qian, J. Irby, S. Banerjee, and A. Tasch, *J. Electron. Mater.* **20**, 309 (1991).

²² M. R. Wertheimer and M. Moisan, *J. Vac. Sci. Technol. A* **3**, 2643 (1985).

²³ M. Moisan, C. Barbeau, R. Claude, C. M. Ferreira, J. Margot, J. Paraszczak, A. B. Sá, G. Sauvé, and M. R. Wertheimer, *J. Vac. Sci. Technol. A* **9**, 8 (1991).

²⁴ C. M. Ferreira and J. Loureiro, *J. Phys. D* **17**, 1175 (1984).

²⁵ M. J. Kushner (private communication, 1991).

²⁶ P. A. Miller, J. T. Verdeyen, and B. E. Cherrington, *Phys. Rev. A* **4**, 692 (1971).

²⁷ H. Yoshida, Y. Morishima, M. Ukai, K. Shinsaka, N. Kouchi, and Y. Hatano, *Chem. Phys. Lett.* **176**, 173 (1991).

²⁸ S. K. Srivastava, AFOSR-AD-A211 367, US Air Force Office of Scientific Research, 1988.

²⁹ *Gmelin Handbuch der Anorganischen Chemie*, edited by Ulrich Krücker (Springer, New York, 1982), Vol. B1, pp. 191–196.

³⁰ D. V. Tsu, Doctoral Dissertation, North Carolina State University, Raleigh, 1989.

³¹ J. Pankove, *Semiconductors and Semimetals* (Academic, New York, 1984), Vol. 21, Part A, Chap. by B. A. Scott.

³² M. J. Kushner, *J. Appl. Phys.* **63**, 2532 (1988).

³³ H. A. Weakliem, R. D. Estes, and P. A. Longeway, *J. Vac. Sci. Technol. A* **5**, 29 (1987).

³⁴ R. Robertson and A. Gallagher, *J. Appl. Phys.* **59**, 3402 (1986).

³⁵ P. S. Skell and P. W. Owen, *J. Am. Chem. Soc.* **94**, 5434 (1972).

³⁶ The $\text{SiH}_2/\text{SiH}_4$ insertion reaction has a reaction probability of 0.99.

³⁷ *Glow-Discharge Hydrogenated Amorphous Silicon*, edited by K. Tanaka (Kluwer Academic, Boston, 1989), Chap. 2.

³⁸ K. Nomoto, Y. Urano, J. L. Guizot, G. Ganguly, and A. Matsuda, *Jpn. J. of Appl. Phys.* **28**, L1372 (1990).

³⁹ S. Veprek, M. Heintze, and F.-A. Sarott, *Mater. Res. Soc. Symp.* **118**, 3 (1988).